

Interfacial Natures and Controlling Morphology of Co Oxide Nanocrystal Structures by Adding Spectator Ni Ions

Jin Seog Gwag[†] and Youngku Sohn^{*}

Department of Chemistry, Yeungnam University, Gyeongbuk 712-749, Korea. *E-mail: youngkusohn@ynu.ac.kr

[†]Department of Physics, Yeungnam University, Gyeongbuk 712-749, Korea

Received October 19, 2011, Accepted December 6, 2011

Cobalt oxide nanostructure materials have been prepared by adding several concentrations of spectator Ni ions in solution, and analyzed by electron microscopy, X-ray diffraction, calorimetry/thermogravimetric analysis, UV-vis absorption, Raman, and X-ray photoelectron spectroscopy. The electron microscopy results show that the morphology of the nanostructures is dramatically altered by changing the concentration of spectator ions. The bulk XRD patterns of 350 °C-annealed samples indicate that the structure of the cobalt oxide is all of cubic Fd-3m Co₃O₄, and show that the major XRD peaks shift slightly with the concentration of Ni ions. In Raman spectroscopy, we can confirm the XRD data through a more obvious change in peak position, broadness, and intensity. For the un-sputtered samples in the XPS measurement process, the XPS peaks of Co 2p and O 1s for the samples prepared without Ni ions exhibit higher binding energies than those for the sample prepared with Ni ions. Upon Ar⁺ ion sputtering, we found Co₃O₄ reduces to CoO, on the basis of XPS data. Our study could be further applied to controlling morphology and surface oxidation state.

Key Words : Co oxide nanostructure, Electron microscopy, X-ray photoelectron spectroscopy, X-ray diffraction, Raman spectroscopy

Introduction

Cobalt oxides have widely been applied to heterogeneous catalysts,¹⁻¹⁰ sensors,¹¹⁻¹⁴ and electrodes.¹⁵⁻¹⁸ Fundamental studies of cobalt oxides have recently been boosted by the desire of achieving an artificial photosynthetic system, and producing clean energy.¹⁹⁻²³ Co₃O₄ with mixed valence states (Co²⁺ and Co³⁺) has been used for CO oxidation.¹⁻⁶ Xie *et al.* prepared Co₃O₄ nanorods, and showed an efficient low temperature CO oxidation and stability.¹ They claimed that the exposed (110) surface planes of nanorods favor Co³⁺ sites which are catalytically more active. Hu *et al.* prepared Co₃O₄ nanosheets, nanobelts, and nanocubes by hydrothermal methods. They showed different methane combustion activities with different crystal planes or morphology (e.g., {112}>{011}>>{001}).⁷ Cobalt oxides have been applied as active materials for sensors.¹¹⁻¹⁴ Nguyen *et al.* prepared porous Co₃O₄ nanorods by a simple hydrothermal method, and showed good sensing properties for volatile molecules such as acetone and benzene.¹¹ Jia *et al.* prepared Co₃O₄ nanowalls, and applied to H₂O₂ detection.¹⁴ As an electrode,¹⁵⁻¹⁸ Xue *et al.* prepared Co₃O₄ nanoneedles directly grown on Cu foils for using Li-ion battery anodes, and found ultrafast charging/discharging rates.¹⁵ For achieving artificial photosynthetic systems, cobalt oxides have played an important role. Jiao and Frei have focused on achieving artificial photosynthetic systems.¹⁹ They prepared Co₃O₄ clusters embedded in mesoporous silica to find an efficient water oxidation property. Uncountable synthetic procedures have been employed to produce highly efficient cobalt oxide materials.²⁴⁻³² It has commonly been known that the effi-

ciency is determined by morphology including size, uniformity, and surface states. Motivated by the earlier literature reports, we have here employed spectator metal ions to tailor the morphologies of Co oxides, and to delve into their physical characteristics.

Experimental Section

The preparation of Co₃O₄ nanostructures is briefly described as follows.¹⁹ Cobalt acetate tetrahydrate (0.01 mol) or cobalt nitrate was completely dissolved in 30 mL ethylene glycol, and the solution was heated to 160 °C. After 0.2 M Na₂CO₃ solution (100 mL) was added, the solution was kept boiling for 1 hour. The final violet precipitates were filtered, washed, dried at 70 °C overnight, and then annealed at 350 °C for 4 hours in air. Nickel nitrate (as spectator metal ions) was introduced into the ethylene glycol solution containing Co precursors. The concentrations of Ni were 0, 1, 3, 5, and 10 mol %. Differential scanning calorimetry/thermogravimetric analysis (DSC/TGA) was taken by using a SDT Q600 thermal analyzer (TA Instruments) at a heating ramp rate of 10 °C/min to 1,000 °C in air. The surface morphology of the oxide samples was imaged by scanning electron microscopy (SEM). Transmission electron microscopy (TEM) images of the samples were recorded using a Tecnai G2 F20 S-TWIN at an acceleration voltage of 200 kV. The specimen was prepared by dropping the Co₃O₄-dispersed ethanol solution onto a carbon-coated Cu grid and drying in air. The UV-vis absorption spectra of Co oxides dispersed in ethanol were taken using a Jasco UV-vis spectrophotometer (V-530). Raman spectra were taken by

using a Bruker Senterra Raman spectrometer (a courtesy of professor K. T. Leung, University of Waterloo, Canada). X-ray diffraction (XRD) patterns of the power samples were taken using a PANalytical X'Pert Pro MPD diffractometer with Cu K α radiation (40 kV and 30 mA) at a take-off angle of 6°. XPS spectra (before and after Ar⁺ ion sputtering) were taken using a Thermo-VG Scientific MultiLab 2000 with a monochromatic Al K α X-ray source (1486.6 eV), a pass energy of 20.0 eV, and a hemispherical energy analyzer.

Results and Discussion

Figure 1(a) and 1(A) show the SEM images of Co oxide nanostructures prepared from Co acetate and Co nitrate solutions, respectively, without adding Ni ions. Figure 1(B)-1(E) are the SEM images of Co oxides prepared by adding spectator Ni ions (1, 3, 5, and 10 mol %) into a Co nitrate solution. As shown in Figure 1(a) and 1(A), we achieved uniform Co oxide nanostructures, with an average size of ~20 nm. As the spectator metal ions increase, the particle size appears to increase, and becomes irregular in size. At a concentration of 10 mol %, the Co oxide nanostructures clearly form a much larger island, compared to Figure 1(A). TEM images were taken for the two selected Co oxide samples prepared without and with 10 mol % Ni ions, shown in Figure 1(A) and 1(E), respectively. The corresponding TEM images are very similar to the SEM images of Figure 1(A) and 1(E). For the sample annealed at 950 °C above the melting point of Co₃O₄, the corresponding SEM image (Figure 1(A)-950 °C) shows large-area flat terraces with a few hundred nm wide.

The XRD patterns of the Co oxide nanostructures are displayed in Figure 2. For the as-prepared un-annealed sample, no clear XRD patterns are shown, indicating a formation of amorphous state. For the 350 °C-annealed samples (a and A-E), all the XRD patterns are commonly in

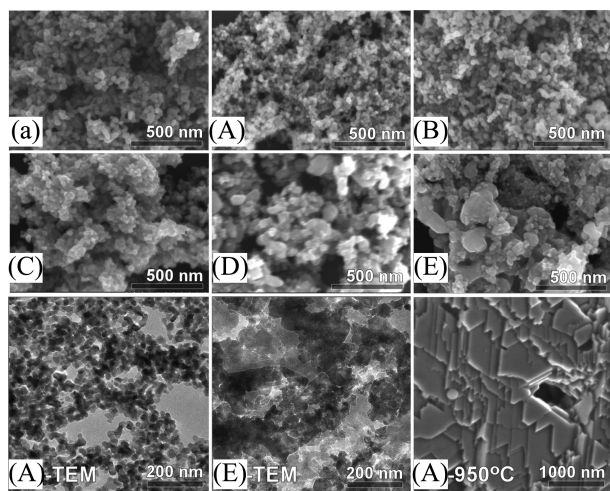


Figure 1. SEM images of Co₃O₄ nanostructures for samples prepared with, (a) Co acetate with no Ni ions, and Co nitrate with, (A) no Ni ions, (B) 1 mol %, (C) 3 mol %, (D) 5 mol %, (E) 10 mol % Ni ions, the corresponding TEM images of samples A and E, and SEM image of 950 °C-annealed sample A.

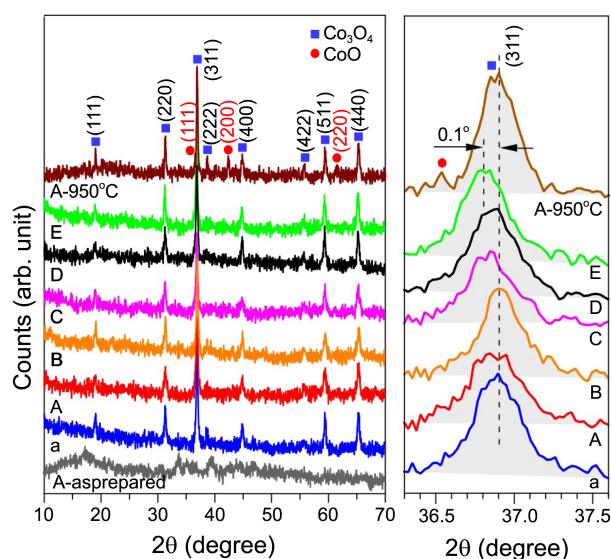


Figure 2. Power X-ray diffraction patterns of Co₃O₄, and expanded (311) XRD peaks.

good accord with those of cubic Fd-3m Co₃O₄ (JCPDS 42-1467). The annealing temperature was determined from a thermo-gravimetric analysis, discussed later. Upon annealing to 950 °C, new XRD peaks appear at 36.5°, 41.4°, and 61.5°, attributed to cubic Fm-3m CoO. The XRD Co₃O₄/CoO ratio is determined to be 85%/15%. The (111), (220), (311), (222), (400), (422), (511) and (440) planes for Co₃O₄, and (111), (200) and (220) planes for CoO are assigned on the peaks. Actually, the XRD patterns (e.g., peak position and width) of the Co₃O₄ samples are very similar, unlike the change in SEM images shown in Figure 1. It appears that although crystalline size is not critically affected by the spectator ions, the particle size is highly affected by the spectator ions, due to an aggregation effect. The crystalline size for Figure 1(A) sample is approximately estimated using the full width at half maximum of the (311) peak and the Scherrer's equation^{32,33} to be 22 nm, in good agreement with the value determined by TEM (Figure 1). For Figure 1a sample, the size was calculated to be 26 nm.

Figure 3 displays the TG/DSC analysis curve of the as-prepared Co sample recorded with a heating rate of 10 °C/

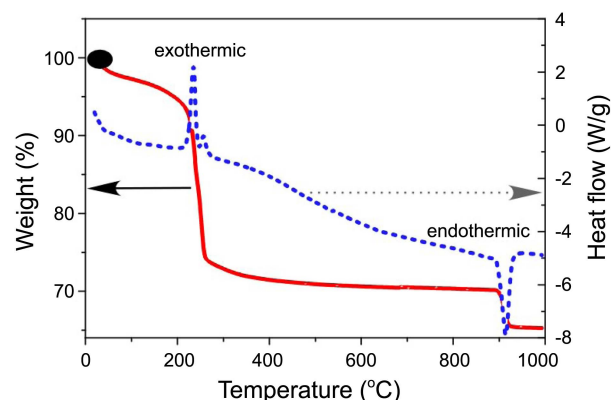


Figure 3. TG/DSC analysis curves of Co oxide sample A.

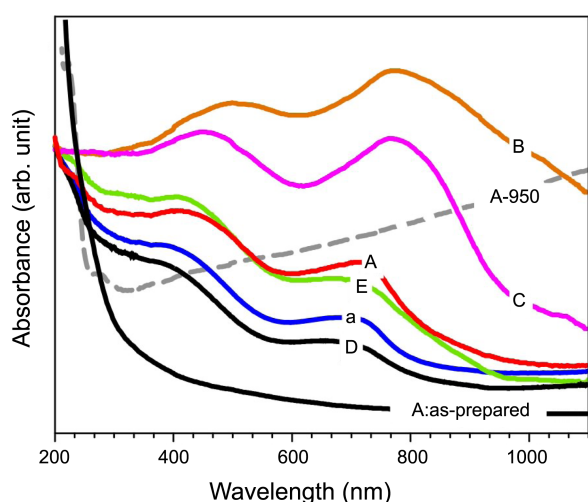


Figure 4. UV-visible absorption spectra of the Co samples dispersed in ethanol.

min in an air condition. At the first stage between room temperature to 210 °C, a gradual decrease in weight occurs, due to removal of adsorbed species such as water molecules. Two sharp large weight losses appear at 235 and 915 °C, consistent with the literature.³⁴ The total weight loss between 210 and 350 °C is estimated to be 22%, attributed to a decomposition reaction forming Co_3O_4 . At above 900 °C showing a sharp endothermic peak, the weight loss is about 4.8%. This is attributed to a thermal decomposition reaction: $\text{Co}_3\text{O}_4 \rightarrow 3\text{CoO} + 1/2\text{O}_2$,³² consistent with the XRD patterns. Actually, the XRD patterns of the 950 °C-annealed sample are largely (85%) due to Co_3O_4 , and partly (15%) due to CoO. From this result, we could assume that hot CoO (achieved upon annealing to 950 °C) phase-changes to Co_3O_4 during cooling to room temperature.³⁵

The UV-visible absorption spectra of Co nanostructures are displayed in Figure 4. As clearly shown, two broad absorption maxima appear at around 400 and 700 nm. Our result is very similar to literature reports.^{36,37} For the as-prepared and 950 °C-annealed samples, no maximum band appears although the 950 °C-annealed sample is mostly Co_3O_4 -form. The former band at 400 nm has been attributed to $\text{O(II)} \rightarrow \text{Co(II)}$ while the latter (700 nm) to $\text{O(II)} \rightarrow \text{Co(III)}$ charge transfers.^{36,37} For the B and C samples, the bands are red-shifted by about 100 nm, plausibly due to a morphology effect. The relative absorption intensity of the two bands could be due to relative formation of Co(III)-O and Co(II)-O sites.³⁶ As a reference, He *et al.* found that as the particle size increases the band shifts to a longer wavelength.³⁶

Figure 5 displays the Raman spectra of the Co oxide nanostructures (shown in Figure 1) at excitation wavelengths of 532 nm (upper) and 785 nm (lower). For the two excitation wavelengths, five major Raman-active modes ($\text{A}_{1g} + \text{E}_g + 3 \text{F}_{2g}$) are commonly found at around 194, 482, 522, 618 and 691 cm^{-1} , assigned to F_{2g} , E_g , F_{2g} , F_{2g} and A_{1g} , respectively.³⁸⁻⁴¹ The assigned peaks are typical characteristics of Co_3O_4 with normal spinel structure (Space group of O_h ,⁷

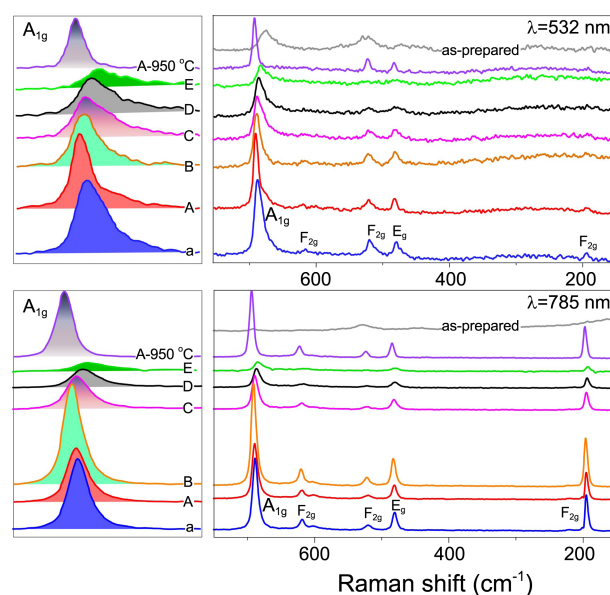


Figure 5. Raman spectra of Co oxides shown in Figure 1, at excitation wavelengths of 532 (top) and 785 nm (bottom). The A_{1g} peak is expanded to show more clearly.

$\text{Fd}\bar{3}m$), where Co^{2+} is positioned at the tetrahedral site while Co^{3+} is located at octahedral site.⁴¹ The dominant A_{1g} peak is attributed to the octahedral site (CoO_6) symmetry, and the weaker F_{2g} peak to the tetrahedral site (CoO_4) symmetry. With increasing the Ni amount during the Co oxide synthesis, the Raman active peak significantly red-shifts, broadens, and becomes weaker. The Raman spectra show a more dramatic change, compared to the XRD results. It appears that the local symmetry becomes distorted, and thereby the crystalline quality becomes degraded. The distortion of the local symmetry could lead a drastic change in Raman peak position. For the 950 °C-annealed sample, the Raman peak of CoO is not clearly discriminated from the entire spectrum. This is plausibly due to that the signal of CoO is relatively weak and superimposable to that of Co_3O_4 .^{39,42} The A_{1g} and F_{2g} ($\sim 195 \text{ cm}^{-1}$) peaks of the 950 °C-annealed sample are blue-shifted by 6 and 2 cm^{-1} , respectively. This is not a surprising result because the morphology of the 950 °C-annealed sample (Fig. 1) and the composition (Fig. 2) are critically different from other samples.³⁹ The peak assignments and positions are summarized in Table 1.

Table 1. Assignments and positions (cm^{-1}) of the Raman peaks taken at an excitation wavelength of 785 nm

Sample \ Assignments	F_{2g}	E_g	F_{2g}	F_{2g}	A_{1g}
a	195.2	480.6	520.3	618.5	688.7
A	195.3	481.2	520.3	618.8	689.4
B	196.2	482.8	522.4	620.3	691.1
C	195.0	482.8	521.2	619.2	689.3
D	194.2	480.1	521.9	616.6	686.7
E	192.9	479.2	523.0	614.2	684.7
A-950 °C	197.3	484.6	523.7	622.7	693.8

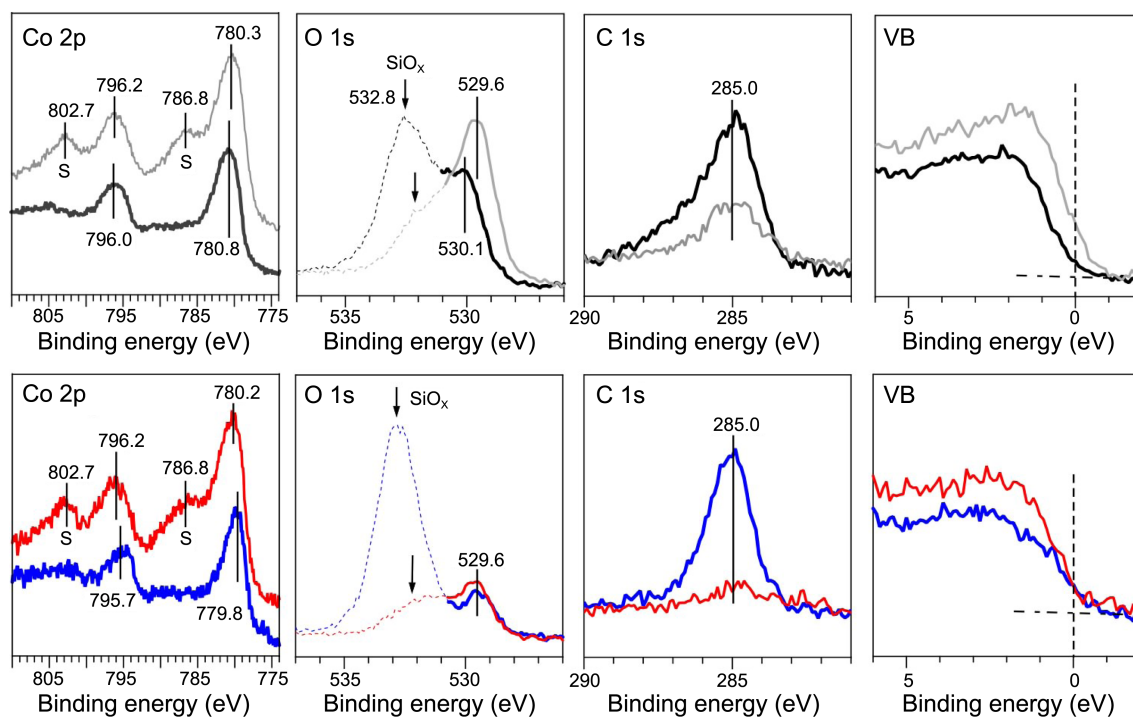


Figure 6. Co 2p, O 1s, C 1s, and VB XPS spectra of Co oxides of Figure 1(A) (top) and Figure 1(E) (bottom) samples. Thicker black (top) and blue (bottom) lines are the spectra before sputtering.

XPS spectra for Co 2p, O 1s, C 1s, and valence band (VB) regions were taken to further elucidate surface chemical compositions and electronic structures. We have selected two different samples (Figure 1(A) and Figure 1(E)) for XPS measurements. Figure 6 displays the corresponding XPS data before and after Ar⁺ ion sputtering. For the sample prepared from the solution containing 10 mol % Ni ions, we could not detect Ni by XPS, indicating that Ni is not loaded over the XPS detection limit. For the Co oxide of Figure 1(A), the Co 2p_{3/2} (2p_{1/2}) XPS peak is observed at 780.8 (796.0) eV, with a spin-orbit splitting of 15.2 eV. The corresponding O 1s peak of the Co oxide is observed at 530.1 eV. The C 1s XPS peak is found at 285.0 eV, attributed surface impurity carbon. The extra O 1s XPS peak at 532.8 eV is mainly due to Si oxides from the Si support (used for mounting the powder samples), and partly due to surface hydroxyl groups.⁴³ These C 1s and O 1s intensities are considerably reduced upon sputtering with no critical change in peak position. To calculate the relative composition of Co versus O for the Figure 1(A) sample, the Co 2p and the corresponding O 1s (530.1 eV) XPS peaks were integrated and divided the intensities by their corresponding relative sensitivity factors ($S_{\text{Co}2p}/S_{\text{O}1s} = 5.43$). The Co/O ratio was calculated to be 1/1.33, or Co₃O_{4.1}. This is in fairly good agreement with the bulk XRD result. Captivatingly, for the XPS of Figure 1E prepared with 10 mol % Ni ions, the Co 2p_{3/2} (2p_{1/2}) XPS peak is positioned at 779.8 (795.0) eV, with a spin-orbit splitting of 15.2 eV. The corresponding O 1s peak is found at 529.6 eV. The calculated Co/O ratio is 1/1.32, or Co₃O₄. For the XPS spectra of the two samples taken after 10 min Ar⁺ ion sputtering, the Co 2p_{3/2} (Co 2p_{1/2})

XPS peak is located at 780.3 (796.2) eV, with a spin-orbit splitting of 15.9 eV. The splitting energy is clearly different from that (15.1 eV) of un-sputtered sample. Furthermore, two strong satellite peaks are found at 786.8 and 802.7 eV. For this reasons, we have assigned the peaks to CoO, consistent with the XPS results of CoO in literatures.^{39,44} The Co 2p with strong satellite peaks have generally been used to identify CoO from other Co oxides. However, the XPS spectra taken after sputtering is inconsistent with the bulk XRD and Raman patterns. This indicates that Ar⁺ ion sputtering induces the formation of CoO from Co₃O₄.³⁹ For the samples (1A and 1E), the VB spectra (between 0 to 5 eV) show that the density of state near the Fermi level increases to some extent upon sputtering, due to a conversion from Co₃O₄ to CoO. Table 1 summarizes some literature Co 2p XPS BE values for more clarification. For Co₃O₄, the spin-orbit (SO) splitting energy of Co 2p_{3/2} and 2p_{1/2} XPS is commonly observed to be about 15.2 eV, in good agreement with our XPS result for Co₃O₄. For CoO and Co hydroxides, the splitting energy is observed to be larger (~16.0 eV), which is in good agreement with our XPS result for CoO achieved upon Ar⁺ ion sputtering.

Before summarizing, we should discuss if Ni is really doped in the Co oxide structure, or just disturbs the crystallinity of the structure to degrade the Raman spectra. Because the Ni amount is extremely small, not detectable by XPS, it is much necessary to confirm it using secondary ion mass spectroscopy (SIMS), inductively coupled plasma-mass spectrometry (ICP-mass), or X-ray fluorescence (XRF). In case that Ni is in the Co oxide structure, the general chemical formula is Ni_xCo_{3-x}O₄, where guest Ni (with

Table 1. Some literature Co 2p XPS BE values for Co oxides

References	Co XPS BEs 2p _{3/2} (2p _{1/2}), and S-O splitting in eV		XPS Instruments, Reference peak
	Co ₃ O ₄	others	
Zheng <i>et al.</i> ⁵	780.4 (795.5), 15.1	-	VG ESCALAB Mk II, C1s=284.6 eV
Petitto <i>et al.</i> ⁴⁴	Co ₃ O ₄ (100): 779.8 (795.7), 15.9, Set to O1s=529.6	CoO(100) 780.5 (796.4), 15.9 Set to O1s=529.4 Strong satellites	Φ15-255G DPCMA
Chen <i>et al.</i> ³⁶	780.0 (795.1), 15.1	-	PHI-5300 ESCA, C1s=284.7 eV
Xu <i>et al.</i> ³⁷	780.0 (795.2), 15.2	-	Kratos AXIS-Hsi, C1s=284.7 eV
Cao <i>et al.</i> ²⁷	779.8 (794.8), 15.0 O1s=530.1	-	C1s=284.7 eV
Wu <i>et al.</i> ¹⁶	Co ₃ O ₄ /graphene 780.2 (795.6), 15.4 O1s=530.1	-	Escalab 250
Barreca <i>et al.</i> ⁴⁵	780.7	CoO: 780.9	Perkin-Elmer Φ5600ci C1s=284.8 eV
Yang <i>et al.</i> ⁴⁶	-	CoOOH: 786.5 (802.4), 15.9 Co(OH) ₃ : 785.7 (801.9), 16.2	Rigaku XPS-7000
This study	780.8 (796.0), 15.2 779.8 (795.0), 15.2	CoO: 780.3 (796.2), 15.9 Strong satellites	MultiLab 2000

oxidation states of both 2+ and 3+) is known to be located preferentially at an octahedral site.⁴⁷ For further detailed local structural analysis, we have a plan to try XANES (X-ray absorption near edge structure) or EXAFS (extended X-ray absorption fine structure). Li *et al.* found that Ni-doping induces an increase in electrical conductivity and roughness.⁴⁷ The roughness could lead broadening, degrading, and shifting of the Raman peaks. In addition, the increase in electrical conductivity could be related with the lower Co 2p XPS BE, at least on the surface state.

Summary

Co oxide nanostructures with different morphologies have been achieved by introducing spectator Ni ions during Co oxide synthesis. The bulk XRD patterns of 350 °C-annealed samples are all of Co₃O₄ showing a slight (0.1°) shift with increasing the concentration of spectator Ni ions. On the basis of TG/DSC analysis, two weight losses appear at 235 and 915 °C, corresponding to the conversions to Co₃O₄ and CoO, respectively. For the XRD patterns of a 950 °C-annealed sample, Co₃O₄ is major while CoO is minor, indicating that CoO converts to Co₃O₄ during cooling to room temperature. We found five Raman active peaks (A_{1g} + E_g + 3 F_{2g}), corresponding to Co₃O₄. The Raman peaks are very sensitive to the samples prepared with different concentrations of spectator Ni ions. For the sample prepared without Ni ions, the XPS spectra reveal that the Co 2p and O 1s BEs are higher than those for the sample prepared with Ni ions. Upon Ar⁺ ion sputtering the XPS spectra for both samples show the same CoO characteristics. This indicates that Ar⁺ ion sputtering induces a conversion from Co₃O₄ to CoO.

Acknowledgments. This research was supported by the

Yeungnam University research grants in 2009.

References

- Xie, X.; Li, Y.; Liu, Z. Q.; Haruta, M.; Shen, W. *Nature* **2009**, 458, 746.
- Liotta, L. F.; Deganello, G.; Di Carlo, G.; Pantaleo, G.; Venezia, A. M. *Curr. Top. Catal.* **2008**, 7, 77.
- Wang, W.; Li, Y.; Zhang, R.; He, D.; Liu, H.; Liao, S. *Catal. Commun.* **2011**, 12(10), 875.
- Xu, C.-X.; Liu, Y.-Q.; Zhou, C.; Wang, L.; Geng, H.-R.; Ding, Y. *ChemCatChem* **2011**, 3(2), 399.
- Zheng, J.; Chu, W.; Zhang, H.; Jiang, C.; Dai, X. *J. Nat. Gas Chem.* **2010**, 19(6), 583.
- Sun, S.; Gao, Q.; Wang, H.; Zhu, J.; Guo, H. *Appl. Catal. B* **2010**, 97(1-2), 284.
- Hu, L.; Peng, Q.; Li, Y. *J. Am. Chem. Soc.* **2008**, 130(48), 16136.
- Li, H.; Fei, G. T.; Fang, M.; Cui, P.; Guo, X.; Yan, P.; Zhang, L. D. *Appl. Surf. Sci.* **2011**, 257(15), 6527.
- Gui, Z.; Zhu, J.; Hu, Y. *Mater. Chem. Phys.* **2010**, 124(1), 243.
- Askarinejad, A.; Bagherzadeh, M.; Morsali, A. *Appl. Surf. Sci.* **2010**, 256(22), 6678.
- Nguyen, H.; El-Safty, S. A. *J. Phys. Chem. C* **2011**, 115(17), 8466.
- Na, C. W.; Woo, H.-S.; Kim, I.-D.; Lee, J.-H. *Chem. Commun.* **2011**, 47(18), 5148.
- Christy, M.; Jisha, M. R.; Kim, A. R.; Nahm, K. S.; Yoo, D. J.; Suh, E. K.; Kumari, T. S. D.; Kumar, T. P.; Stephan, A. M. *Bull. Korean Chem. Soc.* **2011**, 32, 1204.
- Jia, W.; Guo, M.; Zheng, Z.; Yu, T.; Rodriguez, E. G.; Wang, Y.; Lei, Y. *J. Electroanal. Chem.* **2009**, 625(1), 27.
- Xue, X.-Y.; Yuan, S.; Xing, L.-L.; Chen, Z.-H.; He, B.; Chen, Y.-J. *Chem. Commun.* **2011**, 47, 4718.
- Wu, Z. S.; Ren, W.; Wen, L.; Gao, L.; Zhao, J.; Chen, Z.; Zhou, G.; Li, F.; Cheng, H. M. *ACS Nano* **2010**, 4, 3187.
- Guo, B.; Li, C.; Yuan, Z.-Y. *J. Phys. Chem. C* **2010**, 114(29), 12805.
- Wang, X.; Wu, X.-L.; Guo, Y.-G.; Zhong, Y.; Cao, X.; Ma, Y.; Yao, J. *Adv. Funct. Mater.* **2010**, 20(10), 1680.
- Jiao, F.; Frei, H. *Angew. Chem.* **2009**, 121, 1873.
- Park, J. P.; Park, J. Y.; Hwang, C. H.; Choi, M.-H.; Ok, K. M.

- Shim, I.-W. *Bull. Korean Chem. Soc.* **2010**, 31, 2327.
21. Frei, H. *Chimia* **2009**, 63(11), 721.
22. Risch, M.; Khare, V.; Zaharieva, I.; Gerencser, L.; Chernev, P.; Dau, H. *J. Am. Chem. Soc.* **2009**, 131(20), 6936.
23. Wang, G.; Liu, H.; Horvat, J.; Wang, B.; Qiao, S.; Park, J.; Ahnidl, H. *Chem. Eur. J.* **2010**, 16(36), 11020.
24. Li, C. C.; Yin, X. M.; Wang, T. H.; Zeng, H. C. *Chem. Mater.* **2009**, 21(20), 4984.
25. Ma, C. Y.; Mu, Z.; Li, J. J.; Jin, Y. G.; Cheng, J.; Lu, G. Q.; Hao, Z. P.; Qiao, S. Z. *J. Am. Chem. Soc.* **2010**, 132(8), 2608.
26. Zeng, R.; Wang, J.-Q.; Chen, Z.-X.; Li, W.-X.; Dou, S.-X. *J. Appl. Phys.* **2011**, 9(7), 07B520/1.
27. Cao, F.; Wang, D.; Deng, R.; Tang, J.; Song, S.; Lei, Y.; Wang, S.; Su, S.; Yang, X.; Zhang, H. *CrystEngComm* **2011**, 13(6), 2123.
28. Xu, C.; Sun, J.; Gao, L. *CrystEngComm* **2011**, 13(5), 1586.
29. Liang, H.; Raitano, J. M.; Zhang, L.; Chan, S.-W. *Chem. Commun.* **2009**, 48, 7569.
30. Cui, L.; Li, J.; Zhang, X.-G. *J. Appl. Electrochem.* **2009**, 39(10), 1871.
31. Yang, J.; Sasaki, T. *Cryst. Growth Des.* **2010**, 10(3), 1233.
32. Feng, J.; Zeng, H. C. *Chem. Mater.* **2003**, 15, 2829.
33. Langford, J. I.; Wilson, A. J. C. *J. Appl. Cryst.* **1978**, 11, 102.
34. Wang, C.-B.; Lin, H.-K.; Tang, C.-W. *Catal. Lett.* **2004**, 1-2, 69.
35. Gupta, R. K.; Sinha, A. K.; Raja Sekhar, B. N.; Srivastava, A. K.; Singh, G.; Deb, S. K. *Appl. Phys. A* **2011**, 103, 13.
36. He, T.; Chen, D.; Jiao, X.; Wang, Y.; Duan, Y. *Chem. Mater.* **2005**, 17, 4023.
37. Xu, R.; Zeng, H. C. *Langmuir* **2004**, 20, 9780.
38. Zhang, Y. B.; Srirharan, T.; Li, S. *Phys. Rev. B* **2006**, 73, 172404.
39. Gallant, D.; Pezolet, M.; Simard, S. *J. Phys. Chem. B* **2006**, 110, 6871.
40. Hadjiev, V. G.; Iliev, M. N.; Vergilovs, I. V. *J. Phys. C: Solid State Phys.* **1988**, 21, L199-L201.
41. Boucharda, M.; Gambardellab, A. *J. Raman Spectrosc.* **2010**, 41, 1477.
42. Xu, C.; Liu, Y.; Xu, G.; Wang, G. *Chem. Phys. Lett.* **2002**, 366, 567.
43. Sohn, Y. *Appl. Surf. Sci.* **2010**, 257, 1692.
44. Petitto, S. C.; Langell, M. A. *J. Vac. Sci. Technol. A* **2004**, 22, 1690.
45. Barreca, D.; Gasparotto, A.; Lebedev, O. I.; Maccato, C.; Pozza, A.; Tondello, E.; Turner, S.; Tendeloo, G. V. *CrystEngComm* **2010**, 12, 2185.
46. Yang, J.; Hyodo, H.; Kimura, K.; Sasaki, T. *Nanotech.* **2010**, 21, 045605.
47. Li, Y.; Hasin, P.; Wu, Y. *Adv. Mater.* **2010**, 22, 1926.
-